Performance of precast concrete moment frames subjected to column removal: Part 2, computational analysis

Yihai Bao, Joseph A. Main, H. S. Lew, and Fahim Sadek

- This paper presents a computational study of two precast concrete moment-frame assemblies; one was a part of an ordinary moment frame, and the other was part of a special moment frame.
- Each assembly had three columns and two beams and was subjected to displacement-controlled vertical loading of the unsupported center column to simulate a column removal scenario.
- Finite element models of each assembly were developed to evaluate and compare performance of the assemblies.

Ensuring sufficient robustness to resist disproportionate collapse under local damage scenarios is an important consideration in the design of U.S. government and military buildings, as well as prominent privately owned buildings. The alternative load path method, the primary design approach for disproportionate collapse mitigation, requires analyses to demonstrate the adequacy of the structural system to redistribute loads under local damage scenarios, such as loss of columns. Axial forces in beams and their connections can contribute significantly to the redistribution of loads under such scenarios: arching action associated with axial compression can develop in the initial response and catenary action associated with axial tension can develop under large displacements.

Experimental studies are indispensable for characterizing the complex nonlinear behaviors and failure modes resulting from such combined axial and flexural demands and for validation of analysis models for components, connections, and systems. Although extensive research has been devoted to developing and validating numerical models for steel and cast-in-place concrete frame buildings under column removal scenarios,[1–5] there is a lack of published research on alternative load path analysis of precast concrete frame buildings. Corresponding experimental data have also been quite limited, as discussed in the companion paper.[6]

This paper presents computational analyses of two precast concrete moment frame assemblies that were tested under a column removal scenario as described by Lew et al.[6] One assembly was designed as part of an ordinary moment frame, and the other was designed as part of a special moment frame. Each test specimen comprised three columns and two beams, and the specimens were subjected to displacement-controlled vertical loading of the unsupported center column until failure. The footings of the end columns were post-tensioned to the strong floor, and horizontal movements of the end column tops were restrained by a steel frame that simulated the bracing effect provided by the upper stories in a multistory building (Fig. 4 of the companion paper[6]). The moment connections consisted of steel link plates that were welded between embedded plates in the columns and embedded angles in the spandrel beams. Anchorage bars in the spandrel beams were welded to the embedded angles, and failure of both specimens involved fracture of the anchorage bars at the welds.

The three main objectives of this computational study were to develop finite element models that could adequately capture the observed behaviors and failure modes of the specimens; provide additional insights into the behavior and failure modes that could not be directly observed from the experimental data, including the sensitivity of the responses to variations in key factors; and evaluate the structural robustness of the two assemblies by comparing their ultimate capacities with the applicable gravity loading, including the dynamic effects associated with sudden column loss. While the span length of the test specimens was reduced to 25 ft (7.6 m) to fit within the testing facility, computational models with the full prototype span length of 30 ft (9.1 m) were used in the evaluation of structural robustness.

Pretest modeling and model sensitivities

Pretest finite element models of each specimen were developed to aid in planning the tests and laying out the instrumentation. These initial models overestimated the resistance of the test specimens relative to the experimental data and did not capture some of the failure modes that were observed experimentally. The main discrepancies between the pretest model results and the experimental measurements are summarized as follows, along with the key factors that were responsible for the differences.

- Fracture of the welded anchorage bars occurred significantly earlier in the tests than predicted by the pretest models. This earlier fracture was due to localized bending moments near the welds and reductions in the ductility of the anchorage bars in the heat-affected zones near the welds. After the test, component testing of a welded anchorage bar was performed and a more refined posttest modeling approach for the welded anchorage bars was developed to capture these effects, as discussed subsequently.

- Detachment of the column plates and embedded shear studs from the end columns in the ordinary moment frame specimen was not captured by the pretest model. This detachment resulted from a complex state of loading of the shear studs in which shear forces were coupled with tensile forces due to out-of-plane bending of the link plates (Fig. 8 in the companion paper[6]). In the posttest models, the effects of out-of-plane bending were accounted for by reducing the effective shear capacity of the shear studs, as discussed subsequently. While other aspects of the modeling were based on constitutive relationships for the materials, this shear stud failure criterion was

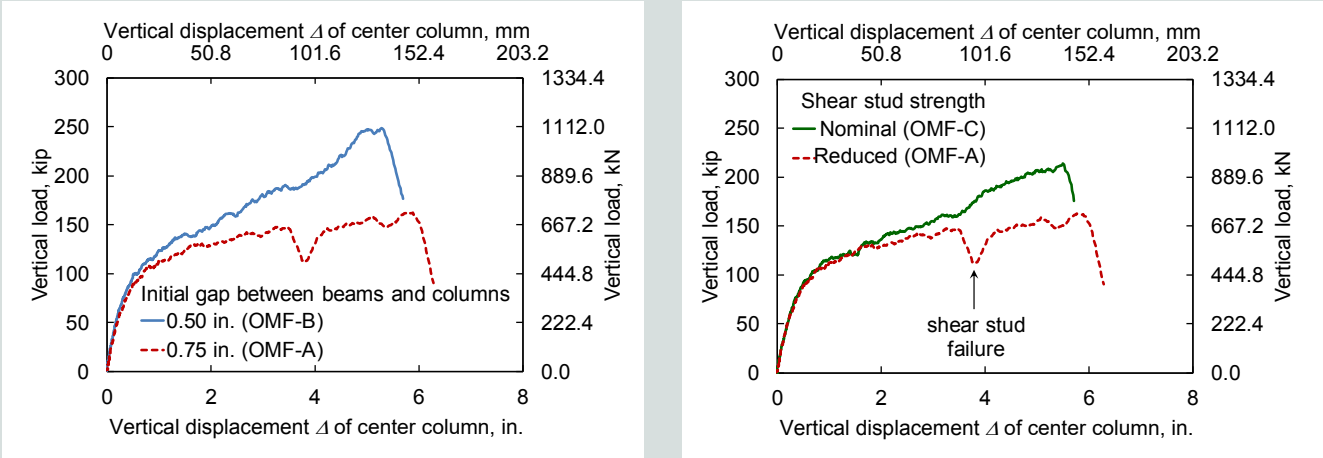

Figure 1. Influence of key factors on computed response of ordinary moment frame specimen. Note: OMF = ordinary moment frame. 1 in. = 25.4 mm.

Table 1. Finite element models used to illustrate the influence of key factors on the computed responses

Model	Initial gap, in.	Shear stud strength	Anchorage bar model
OMF-A*	0.75	Reduced	Ductile
OMF-B	0.50	Reduced	Ductile
OMF-C	0.75	Nominal	Ductile
SMF-A*	0.35	Nominal	Reduced ductility
SMF-B	0.35	Nominal	Ductile
SMF-C	0.5	Nominal	Reduced ductility

Note: OMF = ordinary moment frame; SMF = special moment frame. 1 in. = 25.4 mm.
*Models OMF-A and SMF-A were the final posttest models and are used throughout his paper.

calibrated to capture the experimentally observed failures.

- Development of vertical loads through arching action was less than predicted by the pretest model for the ordinary moment frame specimen. The smaller loads observed experimentally were due to larger initial gaps between the beams and columns than were assumed in the pretest model: the larger gaps delayed the development of arching action and reduced its extent. The gap width was not specified in the design of the prototype buildings, as noted by Main et al.,[7] and a gap width of 0.5 in. (13 mm) was assumed in the pretest modeling. The posttest models used gap widths from the actual test specimens, which were 0.75 in. (19 mm) for the ordinary moment frame specimen and 0.35 in. (9 mm) for the special moment frame specimen. Use of the actual gap widths allowed the posttest models to better capture the experimentally observed arching action.

Figures 1 and **2** illustrate the sensitivity of the computed responses to variations in the key factors mentioned previously by comparing results from three models of each specimen (**Table 1**). Models OMF-A (ordinary moment frame) and SMF-A (special moment frame) were the final posttest models of the two specimens, which are compared with experimental measurements subsequently, while the other models considered variations in key factors (Table 1).

Figure 1 illustrates the influence of the initial gap between the beams and columns on the vertical load-displacement response of the ordinary moment frame specimen. The initial gap width determines the amount of rotation that the connections can accommodate before the gaps close. Once the gaps close, arching action develops in the beams, resulting in significant increases in vertical load accompanied by outward forces on the end columns. The results in Fig. 1 show that increasing the initial gap from 0.5 in. (13 mm) in model OMF-B (as assumed in the pretest modeling) to 0.75 in. (19 mm) in model OMF-A (as estimated directly from the test specimen) reduced the computed ultimate capacity of the specimen by 35%. Figure 1 also shows the influence of reduced shear stud capacity on the computed response of the ordinary moment frame specimen. Model OMF-C included no reduction in the shear stud capacity (as in the pretest modeling), while model OMF-A used a reduced shear capacity, as discussed subsequently. The drop in load at a center column displacement Δ of 3.5 in. (90 mm) for model OMF-A was associated with shear stud failure, and the ultimate capacity of model OMF-A was 24% less than that of model OMF-C. Both factors illustrated in Fig. 1

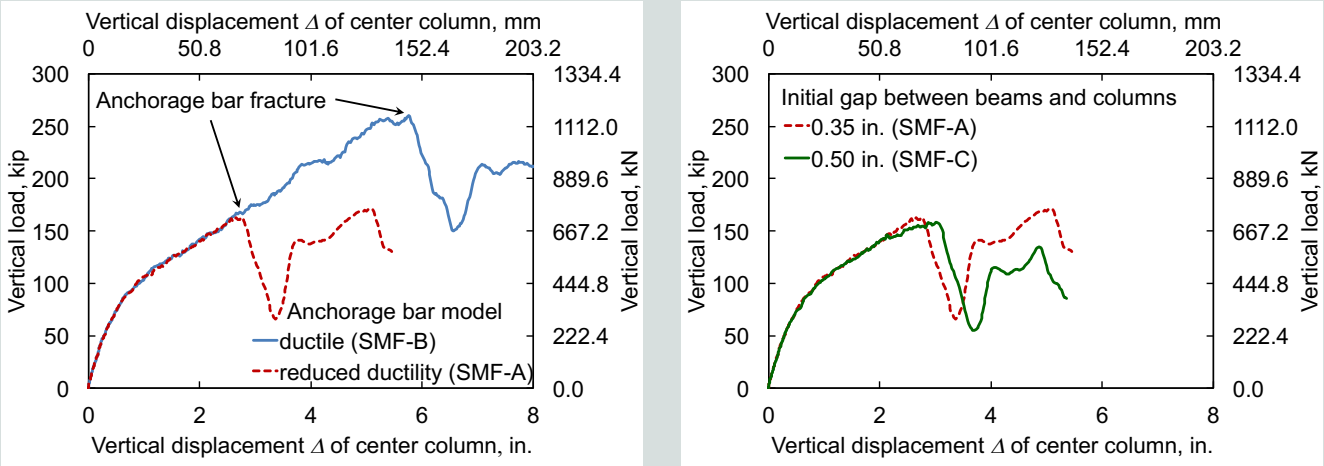

Figure 2. Influence of key factors on computed response of special moment frame specimen. Note: SMF = special moment frame. 1 in. = 25.4 mm.

contributed to the overestimation of the resistance of the ordinary moment frame specimen by the pretest model.

The response of the special moment frame specimen was strongly influenced by the assumed ductility of the anchorage bars near the weld (Fig. 2). Model SMF-B considered no reduction in the ductility of the anchorage bars (as in the pretest modeling), while model SMF-A accounted for reductions in ductility using the approach described subsequently. While fracture of the first anchorage bar occurred at Δ equal to 6.0 in. (150 mm) in model SMF-B, anchorage bar fracture occurred at half of this displacement in model SMF-A, with a corresponding reduction of the ultimate capacity by 37% (Fig. 2).

Figure 2 also shows the influence of the initial gap width on the computed response of the special moment frame specimen. Model SMF-C assumed a gap of 0.5 in. (13 mm) (as in the pretest modeling), while model SMF-A used the average actual gap width of 0.35 in. (9 mm) from the test specimen. The smaller initial gap width in model SMF-A resulted in slightly earlier fracture of the anchorage bars relative to model SMF-C. Model SMF-A also sustained larger vertical loads after anchorage bar fracture than model SMF-C through more extensive arching action resulting from the smaller initial gap. However, the influence of the initial gap width was not as great for the special moment frame specimen as for the ordinary moment frame specimen, and the reduced ductility of the anchorage bars was the primary reason that the pretest model overestimated the resistance of the special moment frame specimen.

Finite element models

Detailed finite element models (**Fig. 3**) were developed to study the behavior and failure modes of the two test specimens. The finite element analyses were conducted using explicit time integration in a general-purpose finite element software package. The analyses accounted for both geometric and material nonlinearities, including modeling the fracture of steel components using element erosion. In the analyses, the center column was pushed downward under displacement control until failure occurred, with displacements increased at a sufficiently slow rate to represent the quasi-static loading conditions of the tests.

Overview

The models used eight-node solid elements to represent the concrete and the steel plates and angles (left side in Fig. 3) and two-node beam elements to represent the reinforcing bars, torsion rods, and shear studs (right side in Fig. 3). The models of the ordinary moment frame and special moment frame specimens consisted of approximately 346,000 elements and 171,000 elements, respectively. More elements were required for the ordinary moment frame specimen because of the greater depth of the spandrel beams. The characteristic length of the solid elements ranged from 0.25 to 2.15 in. (6.4 to 54.6 mm). Typical beam elements ranged from 2.0 to 5.3 in. (51 to 135 mm), with smaller elements in critical regions near the anchorage bar welds (**Fig. 4**) as will be discussed. An automatic contact interface was activated to prevent interpenetration and enable force transfer between the concrete beams and columns and the steel plates and angles.

Shear studs connecting the column plates to the column concrete were modeled using beam elements that shared nodes with the surrounding concrete elements. The nonlinear load-slip behavior of the shear studs was represented through discrete shear springs that connected the beam elements to the column plates (Fig. 4). Welds on the link plates were modeled using constraints that tied the nodes around the edges of the link plates to corresponding nodes on the angles and column plates. Welds between the anchorage bars and the connecting angles were modeled using rigid links to capture the offset between the anchorage bar centerline and the surface of

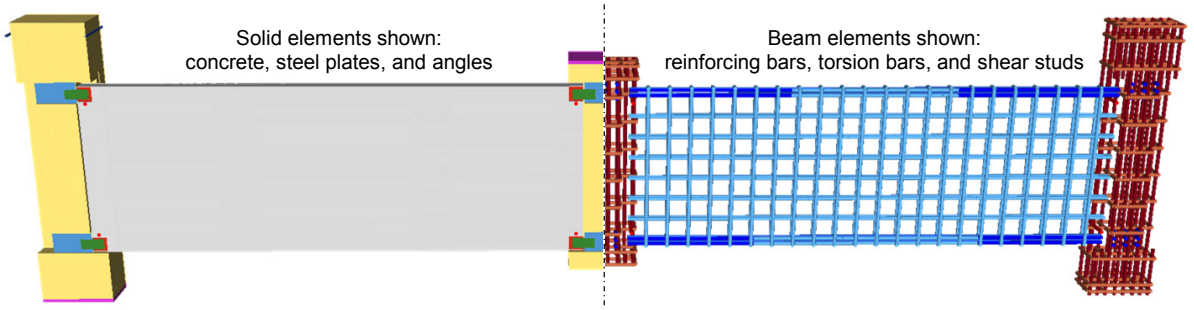

Figure 3. Finite element model (ordinary moment frame specimen).

the connecting angle (Fig. 4). These offsets contributed to the eccentricity in the transfer of forces between the anchorage bars and the link plates, producing significant out-of-plane bending moments in the link plates and in the anchorage bars near the welds. Nodal constraints were used to tie the anchorage bars, as well as the longitudinal and transverse reinforcing bars, to the surrounding concrete elements, and bond-slip effects were neglected. To represent the fixed base conditions for the end columns, all translations were restrained for nodes on the bottom surfaces of steel plates at the column bases. Welding of the column longitudinal bars to the steel base plates was modeled using nodal constraints. Restraint of the end column tops by bracing beams was represented through contact with rigid elements at the inside and outside faces of the end columns. Lateral bracing of the center column and at midspan of the beams was modeled using nodal constraints to prevent out-of-plane displacements.

For consistency with the test, errors in assembly of the special moment frame specimen[6] were represented in the modeling of the special moment frame specimen so that the torsion rods were omitted and the spandrel beams were modeled as inverted, with the longer anchorage bars at the bottoms of the beams rather than at the tops. To investigate the influence of these installation errors, an alternative model (SMF-D), which included torsion rods and noninverted beams and was otherwise equivalent to model SMF-A, was also developed. Comparison of the computed results showed that the influence of the installation errors was small, with a slight delay in fracture of the welded anchorage bars for model SMF-D relative to model SMF-A and an increase of the ultimate vertical load by 3.5%.

Material modeling

This section summarizes the modeling approaches and material properties used for the various components of the test specimens. Further details, including stress-strain curves used in the modeling, are provided in National Institute of Standards and Technology (NIST) Technical Note 1886.[7]

Concrete A continuous surface cap plasticity model[8] was used as the material model for concrete. Key features of the model include isotropic constitutive equations, a yield surface formulated in terms of three stress invariants with translation for prepeak hardening, a hardening cap that expands and contracts, and damage-based softening with modulus reduction in both compression and tension. The model captures confinement effects and uses a constant fracture energy approach to regulate mesh size sensitivity in the modeling of softening behavior. Using initialization routines provided in the model, material model parameters were fit to experimental data based on the average measured 28-day compressive strength of 5785 psi (39.89 MPa) for the precast concrete specimens. Reduced-integration solid elements were used to model the concrete, and spurious zero-energy modes of deformation were suppressed using an assumed strain corotational stiffness form of hourglass control with an hourglass control coefficient of 0.03.

Steel plates and angles A piecewise linear plasticity model was used as the material model for the ASTM A36[9] steel plates and angles, which were modeled using fully integrated solid elements. A representative stress-strain curve was used for the steel plates and angles, based on tensile testing of ASTM A36 steel coupons reported by Sadek et al,[10] with a yield strength of 42 ksi (290 MPa), an ultimate tensile strength of 65 ksi (450 MPa), and an engineering strain of 22% at the ultimate tensile strength. The engineering stress-strain curve obtained from tensile testing was converted to a true stress–versus–plastic strain curve as required by the material model, and postultimate softening and fracture were considered as described by Main et al.[7] However, the postultimate modeling approach for the steel plates and angles had a negligible effect on the computed results because fracture did not occur in these components.

Reinforcing bars Similar to the steel plates and angles, a piecewise-linear plasticity model was used for the ASTM A706[11] Grade 60 (410 MPa) reinforcing bars, which were modeled using beam elements with cross-section integration. A distinct material model was defined for each size of reinforcing bar used in the test specimens, with stress-strain curves for each bar size based on data from tensile testing reported by Main et al.[7] Modeling of critical regions of the anchorage bars near the welds used a different approach that is explained subsequently.

Torsion bars The torsion bars, which were ASTM A193[12] Grade B7 bolts, were modeled using the same piecewise linear plasticity material model and beam element formulation that were used for the reinforcing bars. Modeling of the torsion bars assumed that the ultimate tensile strength was equal to the minimum specified value of 125 ksi (862 MPa), with a yield strength of 100 ksi (700 MPa) and an engineering strain of 0.08 at the ultimate tensile strength. A simple bilinear form of stress-strain curve was assumed. To model the pretension introduced in the torsion bars during the assembly process, a coefficient of thermal expansion was defined in the material model and the torsion bar elements were artificially cooled to develop tensile stresses through restraint of thermal contraction. Several trial analyses were performed to determine the reduction in temperature required to achieve the desired service tension of 18 kip (81 kN), as listed in the *PCI Design Handbook: Precast and Prestressed Concrete*.[13]

Shear studs Discrete shear springs (Fig. 4) were used to represent the nonlinear shear behavior of the shear studs that connected the column plates to the column concrete. The normalized shear force versus slip relationship used for the shear springs was based on the empirical load-slip relationship proposed by Ollgaard et al.[14] for slip displacements up to 0.2 in. (5 mm), which corresponds to the peak shear force. After reaching the peak load, the shear force was gradually reduced to 80% of its peak value at a displacement of 0.4 in. (10 mm) and was then steeply reduced to a constant residual strength equal to 20% of its peak value. This residual strength represents the frictional resistance of crushed concrete that remains even after failure of a shear stud.

For the 1.0 in. (25 mm) diameter shear studs used in the ordinary moment frame and special moment frame connections, a nominal shear strength Q_n of 38 kip (170 kN) was calculated based on the American Institute of Steel Construction's (AISC's) *Specification for Structural Steel Buildings* section I8.2a,[15] assuming an ultimate tensile strength of 65 ksi (450 MPa) for the shear studs, which is the minimum specified tensile strength for American Welding Society D1.1 Type B studs.[16] This nominal shear strength was used in the model of the special moment frame specimen and no shear stud failure occurred, consistent with the experimental results. However, using this nominal shear strength for the ordinary moment frame specimen failed to capture the experimentally observed detachment of the upper column plates from the end columns and significantly overestimated the vertical load sustained by the ordinary moment frame specimen (model OMF-C in Fig. 1).

Detachment of the column plates in the ordinary moment frame specimen involved significant out-of-plane displacement, which resulted from out-of-plane bending of the link plates (Fig. 8 of the companion paper[6]). The shear studs were thus subjected a complex state of loading that involved not only shear forces but also axial tension, and this tension reduced the effective shear capacity of the shear studs. This effect was more significant for the ordinary moment frame specimen than for the special moment frame specimen because of the more extensive out-of-plane bending of the link plates that occurred.

Developing a failure model for the shear studs that explicitly accounts for the complex interaction of stresses observed here would require further research and is beyond the scope of this study. The key observation is that these effects reduced the effective shear capacity of the shear studs, and accounting for this reduction was necessary to capture the experimentally observed failures. In model OMF-A (the final posttest model), an effective shear strength of 12 kip (53 kN) was used for the shear studs, which represents only 31% of the nominal shear strength. This value was calibrated to the experimental data to capture the column plate detachment observed at a center column displacement Δ of 3.7 in. (89 mm). Measured anchorage bar forces confirmed that failure of the shear studs in the ordinary moment frame specimen occurred under shear forces that were well below the nominal shear strength.[7]

Welded anchorage bar modeling

This section describes the modeling approaches that were used to account for the two key factors mentioned previously that influenced the fractures of the welded anchorage bars: localized bending moments near the welds and reductions in the ductility of the anchorage bars in the heat-affected zone near the welds. The first of these factors was significant for both the ordinary moment frame and special moment frame specimens, while the second factor was significant only for the special moment frame specimen. Section 6.7.3 of the *PCI Design Handbook*[13] notes that welding reinforcing bars can potentially result in crystallization, associated with brittle behavior, and discusses preheat and other requirements to avoid such effects.

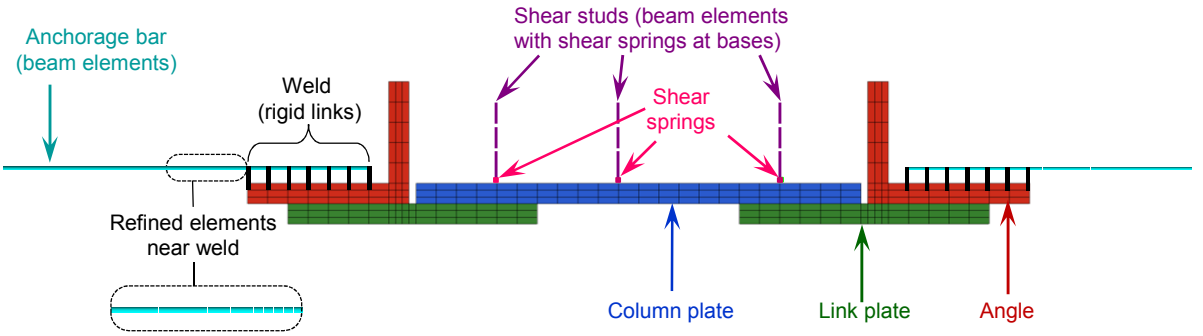

Figure 5. Modeling details at moment connection (top view, special moment frame specimen).

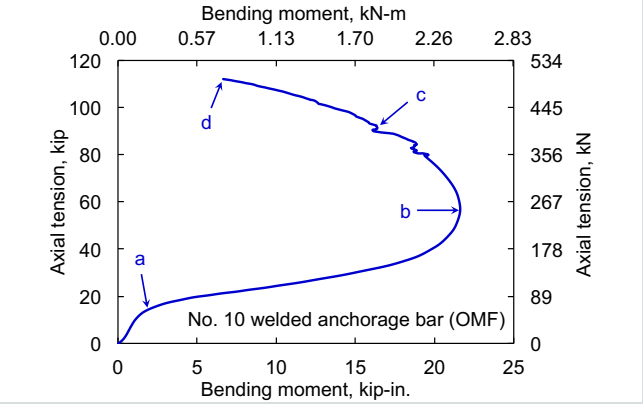

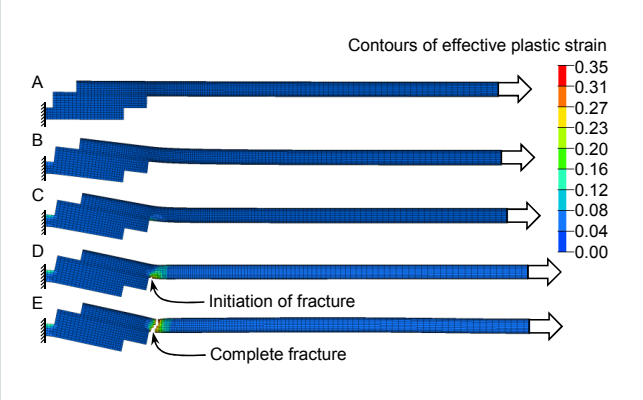

Figure 5. Modeling details at moment connection (top view, special moment frame specimen).

Weld-induced reductions in ductility of the anchorage bars may have been more significant for the special moment frame specimen than for the ordinary moment frame specimen because of the greater heat input associated with the larger weld size. Variability in the welding process may also have contributed to the differences in ductility because, even for the special moment frame specimen, reductions in ductility seem to have been more significant for the lowest anchorage bar at the center column, which fractured first, than for the upper two anchorage bars at the same location, which fractured significantly later.[6] In the computational modeling of each specimen, all anchorage bars were assumed to have the same ductility, and consequently, fracture of the anchorage bars was essentially simultaneous for all bars at a given location.

Interaction of bending moment and axial force

Experimental measurements[6] have indicated that the welded anchorage bars were subjected to a combination of bending and axial loading due to eccentricities in the transfer of forces between the link plates and the anchorage bars. The resulting interaction of bending moment and axial tension caused the anchorage bars to fracture at a lower axial force than if the bars had been subjected to pure tension. Because detailed modeling of the welded anchorage bars using solid elements would be too computationally demanding for analysis of an entire test specimen, a reduced-order modeling approach was used (Fig. 4) in which the welded anchorage bars were modeled using beam elements. However, detailed solid-element models of welded anchorage bars under eccentric loading were also developed (**Fig. 5**) to verify the adequacy of the reduced-order modeling approach and to enable calibration of the failure criterion used to model bar fracture.

The welded anchorage bar models used for calibration included a single anchorage bar along with strips of angle and link plates having widths obtained by dividing the actual widths by the number of anchorage bars in the connection. Concrete was excluded from the models because the focus of these analyses was on the transfer of tensile forces through the steel components at the welded connections. Solid elements representing welds in the detailed model used the same material model as for the anchorage bars. In both the detailed and reduced-order models, the welds between the angle and the link plate were modeled by having elements of the two components share common nodes at their interface. Only the angle leg parallel to the link plate was included in the models because the perpendicular leg was not loaded in the configuration being analyzed. The portion of the link plate that was welded to the column plate was not included in the model. Instead, the link plate was truncated at the edge of the column plate, and this truncated end was modeled as fixed. A segment of anchorage bar extending 30 in. (760 mm) beyond the end of the angle was modeled, and displacement-controlled axial loading was applied to the end of this bar segment. Eccentricity in the loading resulted from the offset (in the direction normal to the link plate) between the load applied to the anchorage bar and the reaction at the fixed end of the link plate.

To capture this localized bending of the anchorage bars in the reduced-order models, a refined mesh was required near the weld (Fig. 4). After considering various mesh sizes in this refined zone, a beam element length of 0.2 in. (5 mm) was selected and was found to be sufficient to capture the maximum bending moment at the end of the weld as well as the decay in bending moment along the length of the bar. The nonlinear distribution of axial stress over the cross section of the bar was captured using 64 integration points per element. Fracture was modeled using element erosion at a specified value of plastic strain, which was

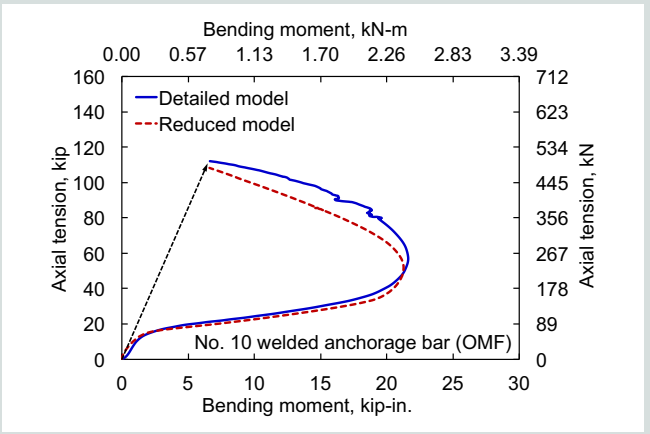

Figure 6. Interaction of axial force and bending moment for welded anchorage bars under eccentric loading. Note: OMF = ordinary moment frame; SMF = special moment frame. No. 10 = 32M; no. 11 = 36M.

calibrated against the detailed models. First, the erosion strain used to model fracture in the detailed models was calibrated to match the elongation at fracture from tensile testing of no. 10 and 11 (32M and 36M) bars, as described by Main et al.[7] Then the failure criterion used in the reduced-order models was calibrated against the detailed models using the welded anchorage bar models (Fig. 5).

Figure 5 shows computed results from the detailed model of a welded no. 10 (32M) bar. The interaction diagram of axial tension versus bending moment is plotted, and for the points labeled on the interaction diagram, the corresponding deformed geometry of the finite element mesh is shown with contours of effective plastic strain. Plastic strains were concentrated in the link plate near the fixed end and in the anchorage bar near the end of the weld. The final point on the interaction diagram (point D) corresponds to the initiation of fracture at the peak axial load. Figure 5 also shows the deformed shape after complete fracture.

The values of bending moment plotted in Fig. 5 were calculated for the cross section at the end of the weld, where the bending moment was largest. The computational results showed that the bending moment decayed steeply with distance along the bar. At an axial tension of 57.1 kip (254 kN), corresponding to point B in Fig. 5, the bending moment decayed to 50% of its peak value 3.3 in. (84 mm) from the end of the weld. At an axial tension of 91.4 kip (407 kN), corresponding to point C in Fig. 5, the bending moment decayed even more steeply, dropping to 50% of its peak value only 0.8 in. (20 mm) from the end of the weld.

Figure 6 shows a comparison of moment-axial interaction diagrams obtained using the detailed and reduced models of both no. 10 (32M) and no. 11 (36M) welded anchorage bars under eccentric loading. For each bar size, the erosion strain used in the reduced model was calibrated so that the detailed and reduced models had approximately the same ratio of bending moment to axial force at the fracture point. Graphically, this required the fracture points for the detailed and reduced models to lie approximately along the same ray directed from the origin, as indicated with the dashed arrow annotation in Fig. 6. This calibration approach was adopted to best match the degree of moment-axial interaction at the point of fracture, rather than seeking to match either the bending moment or the axial force at the expense of the other. The results show good agreement between the interaction diagrams obtained using the detailed and reduced modeling approaches. The peak bending moment and the peak axial force both agree within 6% for the no. 10 bar and within 9% for the no. 11 bar. This good agreement confirmed that the reduced modeling approach can capture the interaction of bending moment and axial tension leading to fracture of the anchorage bars.

Reduction of ductility in heat-affected zone

When the calibrated, reduced-order model of the welded no. 10 (32M) anchorage bar (Fig. 6) was implemented in analysis of the ordinary moment frame specimen, the model closely captured the center column displacement at which anchorage bar fracture occurred. In contrast, when the calibrated, reduced-order model of the welded no. 11 (36M) anchorage bar (Fig. 6) was implemented in analysis of the special moment frame specimen (model SMF-B), anchorage bar fracture in the model occurred significantly later than observed experimentally. To investigate the cause of the earlier anchorage bar fracture observed experimentally, component testing of a welded anchorage bar from the special moment frame specimen was performed (**Fig. 7**).

The welded anchorage bar connection used in the component test was recovered from a location in the tested special

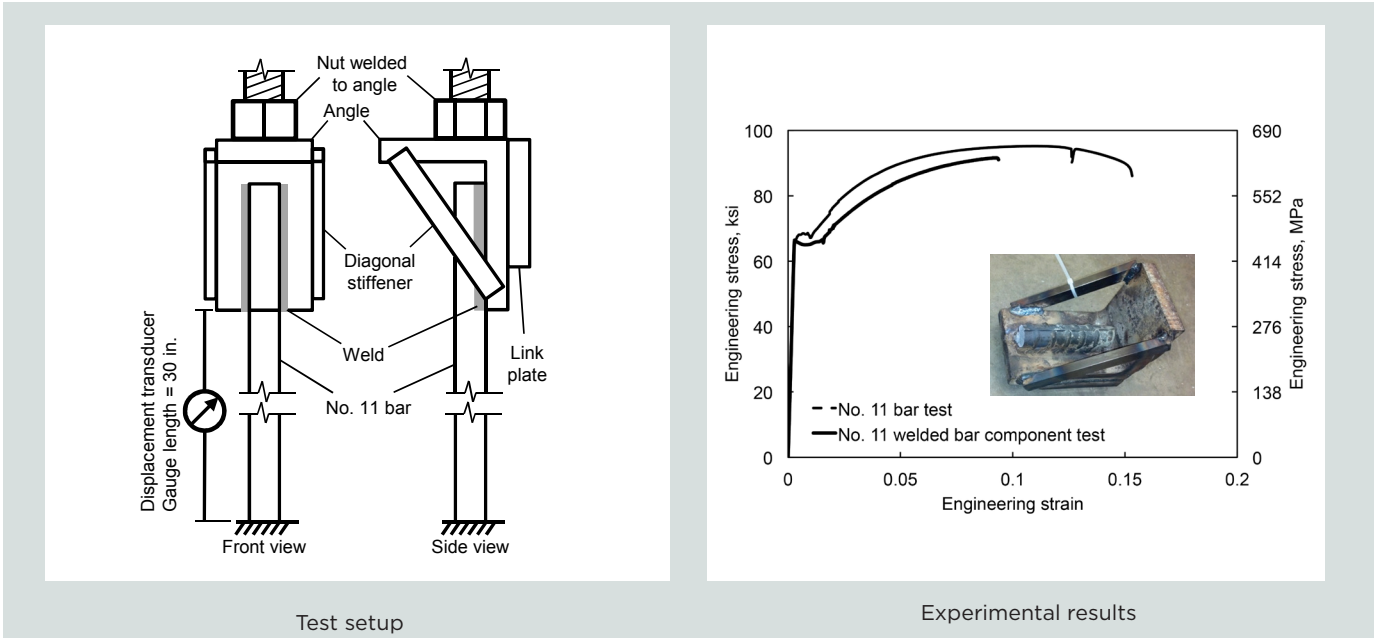

Figure 7. Component testing of welded anchorage bar. Note: No. 11 = 36M. 1 in. = 25.4 mm.

moment frame specimen that was subjected to predominantly compressive loads during the test. The three-bar connection was sawed through the angle and link plate to isolate a single anchorage bar for testing, along with a strip of angle with a width of 4.5 in. (110 mm) welded to the no. 11 (36M) bar. The angle and link plate were welded together along the sawed edge, and the link plate was also sawed flush with the heel of the angle. A nut was welded to the perpendicular leg of the angle to receive a 2 in. (50 mm) diameter threaded rod, through which tensile loading was applied in the testing machine (Fig. 7). The nut was aligned along the axis of the anchorage bar to provide concentric axial loading.

Steel bars with dimensions of 8 × 1 × 0.5 in. (200 × 25 × 13 mm) were welded diagonally between the two legs of the angle to stiffen the angle and prevent out-of-plane deformations. Elongations of the anchorage bar were measured using a displacement transducer spanning a gauge length of 30 in. (760 mm) and attached to the toe of the angle at the end of the weld. The welded anchorage bar was tested under displacement-controlled tensile loading until fracture occurred. The estimated uncertainty in the measured load and displacement data was ±1%.

Figure 7 shows a comparison of the stress-strain curve obtained from the welded-bar component test with the stress-strain curve obtained from tensile testing of a no. 11 (36M) bar. The yield stress is almost equivalent in both cases, and the welded bar showed only slightly lower stress in the postyield work-hardening phase. However, the welded bar had significantly reduced ductility, with the ultimate stress being reached at an engineering strain of 9.3% and fracture occurring immediately thereafter without appreciable necking. In contrast, the ultimate stress was reached at an engineering strain of 11.1% in the bar tensile test and was followed by significant necking and softening prior to fracture.

The inset of Fig. 11 shows the fractured anchorage bar after the component test, in which it is evident that the fracture occurred at the end of the weld. The reduced ductility of the welded anchorage bar is believed to have been caused by changes in material properties in the heat-affected zone near the weld (for example, microstructural changes such as the formation of brittle martensite).

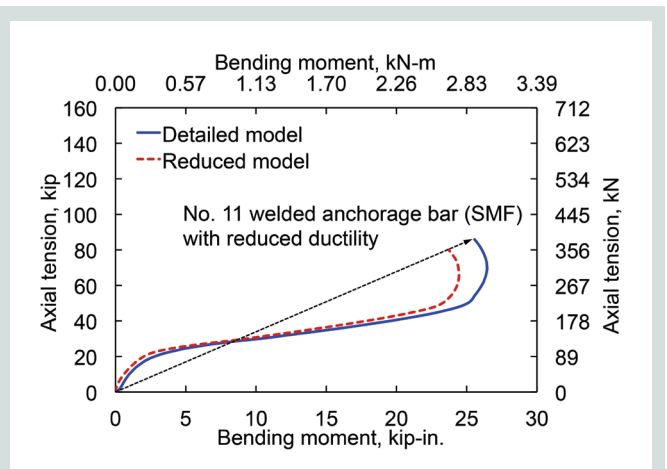

Figure 8. Interaction of axial force and bending moment for a welded no. 11 (32M) anchorage bar under eccentric loading, including a reduction in ductility due to welding. Note: SMF = special moment frame.

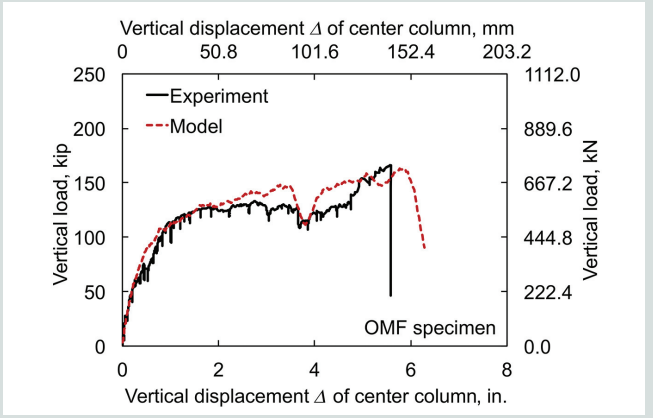

Vertical load

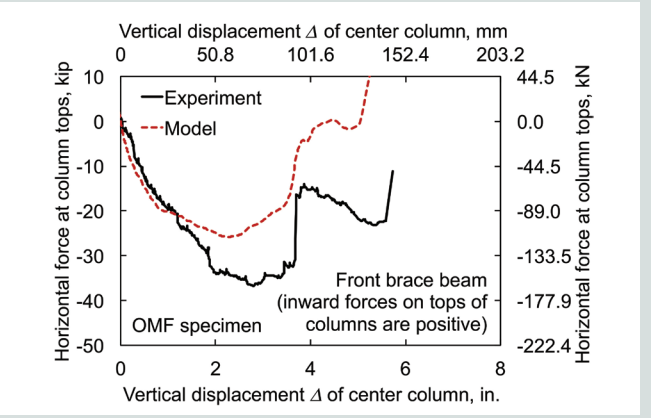

Horizontal reaction at column tops

Figure 9. Comparison of experimental and computed results for ordinary moment frame (OMF) specimen.

Based on the results of the welded bar component test, the reduced model of the welded no. 11 (32M) anchorage bar (Fig. 6) was recalibrated to account for the reduced ductility that was observed. This recalibration followed the same procedure outlined in the previous section but with one modification; rather than calibrating the anchorage bar material model against a bar tensile test, the material model was instead calibrated against the welded bar component test. This calibration used a detailed model of the welded bar component test that was similar to that in Fig. 5, except that the boundary conditions were modified to represent the concentric loading conditions in the test. To represent the reduced ductility in the heat-affected zone near the weld, element erosion was activated only for anchorage bar elements adjacent to the weld and within one row of elements beyond the end of the angle. The erosion strain was calibrated to match the experimental engineering strain at fracture (Fig. 7).

After calibrating the anchorage bar material model against the welded bar component test, the welded bar was analyzed again under the eccentric loading and support conditions illustrated in Fig. 5. **Figure 8** shows the resulting moment-axial interaction diagram along with corresponding results from the reduced model. Like in Fig. 6, the erosion strain used in the reduced model was calibrated so that the detailed and reduced models had approximately the same ratio of bending moment to axial force at the fracture point. Comparing Fig. 8 with Fig. 6 reveals that the reduction in ductility due to welding led to a 35% reduction in the peak tensile force that could be sustained under eccentric loading. Because the tensile capacity from the welded bar component test (under concentric loading) was only 4% less than that of the bar without welding (Fig. 7), this shows that moment-axial interaction under eccentric loading can amplify the effects of reduced ductility. This helps to explain why the ultimate capacity of model SMF-A,

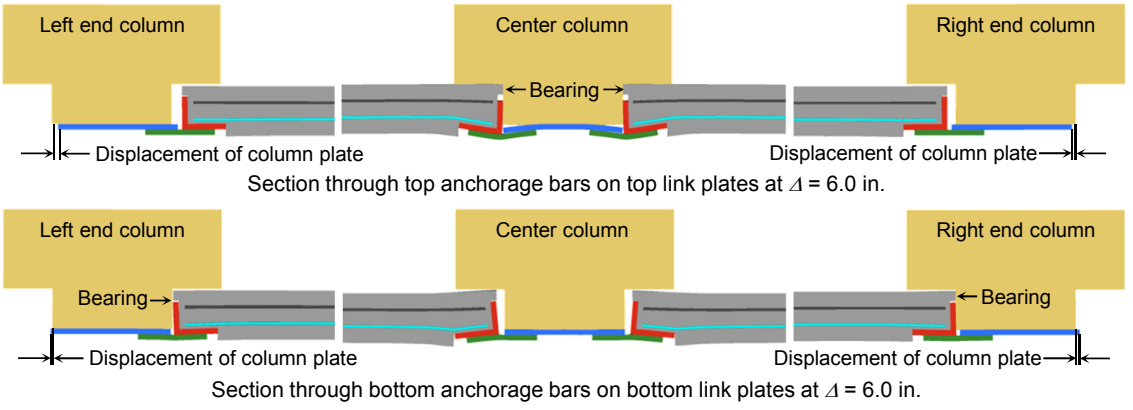

Figure 10. Section views of ordinary moment frame model near the peak vertical load. Note: Δ = vertical displacement. 1 in. = 25.4 mm.

which had anchorage bars with reduced ductility, was so much less than that of model SMF-B, which had ductile anchorage bars (Fig. 2).

Analysis of test specimens

This section presents analysis results from the final posttest models of each test specimen (models OMF-A and SMF-A in Table 1), including comparisons with experimental measurements. In the analysis of each specimen, self-weight loading was first applied gradually and then held constant for the rest of the analysis by imposing a body-force-acceleration–versus–time curve. After the specimen reached an equilibrium configuration under its own self-weight, the unsupported center column was pushed downward by prescribing a gradually increasing velocity-versus-time curve to the steel loading plate at the top of the center column. Loads were transmitted to the center column through contact with the steel loading plate, consistent with the experimental configuration.

Ordinary moment frame specimen

Figure 9 shows a comparison between the measured and computed curves of the applied vertical load and the horizontal reaction force at the end column tops for the ordinary moment frame specimen, both plotted against the vertical displacement of the center column. A slight drop in both the measured and computed vertical load is evident in Fig. 13 at a center column displacement Δ of 3.7 in. (89 mm), corresponding to shear stud failure at the top column plates on the end columns. Because of this failure, a more severe drop occurred in both the measured and computed horizontal reaction from the front brace beam at the tops of the end columns (Fig. 9).

Inward horizontal forces on the column tops are considered positive in Fig. 9, corresponding to tension in the brace beam spanning between the tops of the end columns. The experimental curve for the horizontal force in Fig. 9 corresponds to the axial force in the front brace beam calculated based on measured strain data. While the brace beams themselves were not included in the computational model, their influence was represented through contact with rigid elements at the inside and outside faces of the end column tops.

For consistency with the experimental measurements, the curve from the computational model in Fig. 9 represents the portion of the horizontal reaction that would have been transferred to the front brace beam. The computed horizontal reactions at the tops of the two end columns were averaged, with inward forces positive. (The horizontal reactions at the two end column tops were essentially equivalent initially, but differences became evident after shear stud failure occurred and the response was no longer symmetric.) An outward horizontal reaction developed in the initial application of self-weight in the computational model, and for consistency with the experimental measurements, this initial reaction was deducted from the horizontal force values in Fig. 9. The peak computed horizontal reaction from the front brace beam prior to shear stud failure was 29% less than the peak force from the experimental data. Despite this discrepancy in the peak brace force, the initial development of compressive forces was captured by the model, as was the reduction in force associated with shear stud failures.

Shear stud failures were evident in the computational model by increased displacements of the top column plates relative to the end columns (**Fig. 10**). Figure 10 shows section views of the ordinary moment frame model at a center column displacement Δ of 6.0 in. (150 mm), near the peak vertical load. Figure 10 shows section views at the level of the top anchorage bars on the top link plates and at the level of the bottom anchorage bars on the bottom link plates. As discussed, shear stud failures in the ordinary moment frame specimen were influenced by out-of-plane bending of the link plates, and significant out-of-plane bending of

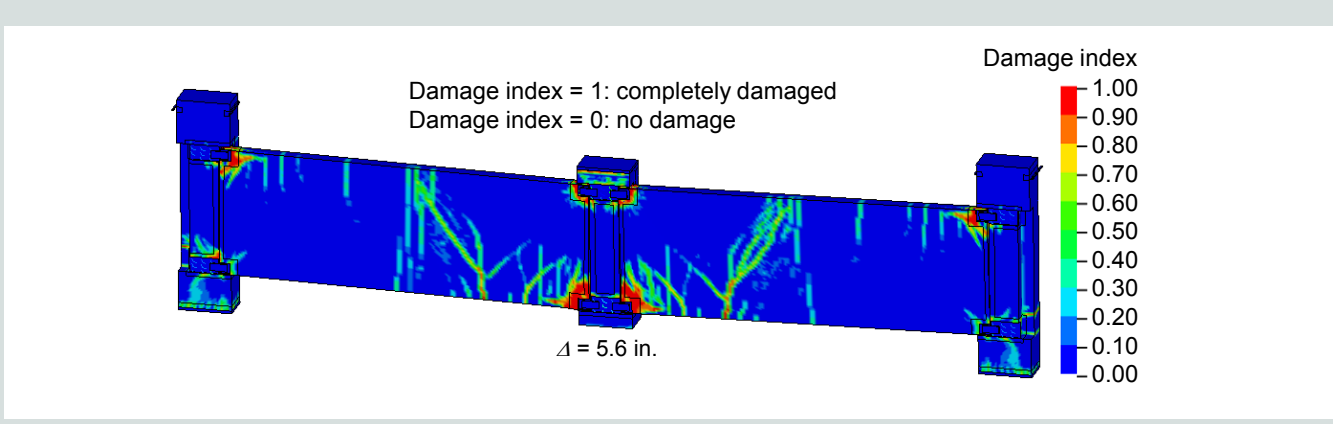

Figure 11. Concrete damage for ordinary moment frame specimen prior to anchorage bar fracture. Note: Δ = vertical displacement. 1 in. = 25.4 mm.

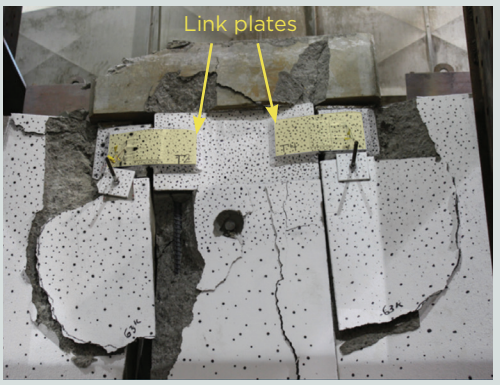

Ordinary moment frame damage

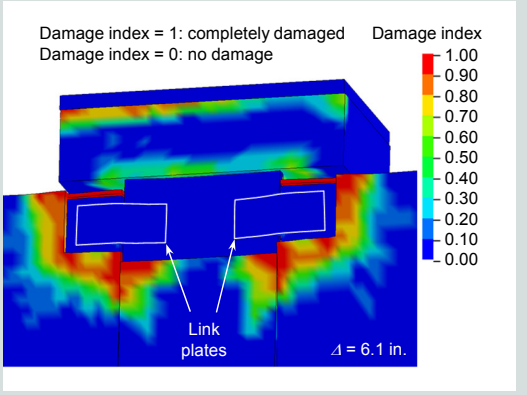

Contours of computed damage index

Figure 12. Concrete damage near top of center column for ordinary moment frame specimen after anchorage bar fracture. Note: Δ = displacement. 1 in. = 25.4 mm.

the link plates is evident in Fig. 10, particularly at the center column, where balanced forces from the beams on each side prevented shear stud failures.

After shear stud failures occurred, the ordinary moment frame specimen developed additional capacity through arching action, with the top ends of the beams bearing against the center column, and the bottom ends of the beams bearing against the end columns (Fig. 10). Figure 11 presents contours of the concrete damage index near the peak vertical load and shows that concrete damage was concentrated in the regions surrounding the beam-to-column connections and in the lower portions of the end columns. Between the connections, the spandrel beams exhibited a predominantly linear deflected profile, consistent with the experimental measurements. Shortly after the onset of arching action, which was evidenced by bearing of the beams against the columns, inclined damage contours developed in the lower portions of the end columns. These inclined damage contours indicated the formation of diagonal shear cracks consistent with the experimental observations.

Figure 12 shows the concrete damage near the top of the center column, a location where extensive spalling occurred, comparing a photograph taken after the peak vertical load with damage contours from the computational model at Δ equal to 6.1 in. (155 mm), also after the peak vertical load. While the concrete damage model is unable to capture discrete cracking and spalling, the concentration of damage around the link-plate connections in the computational model is generally consistent with the damage in the ordinary moment frame specimen. Out-of-plane bending of the link plates is evident in Fig. 12, and the deformed shape of the link plates in the computa-

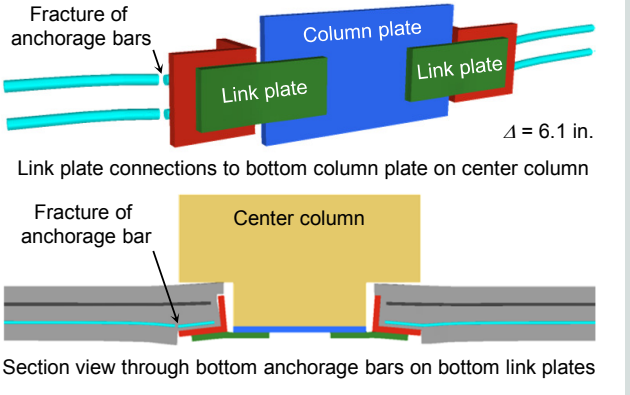

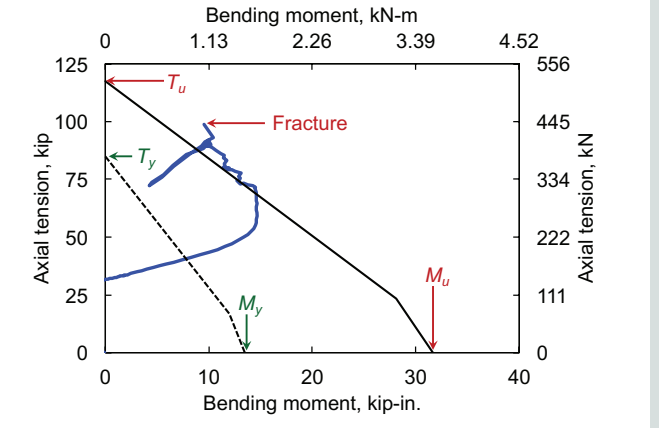

Interaction of axial force and bending moment

Figure 13. Anchorage bar fracture in ordinary moment frame model. Note: M_u = ultimate moment; M_y = yield moment; T_u = ultimate capacity in tension; T_y = yield capacity in tension; Δ = vertical displacement. 1 in. = 25.4 mm.

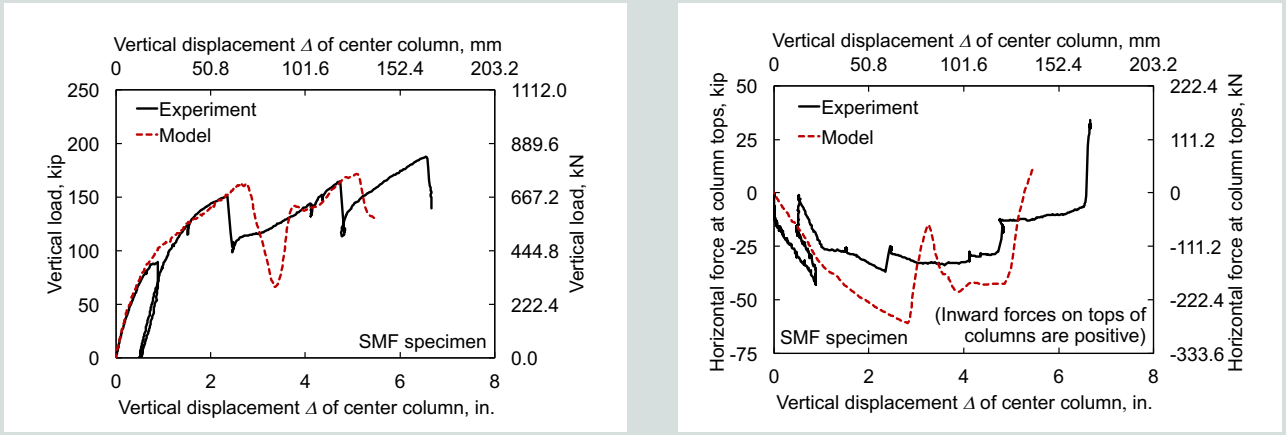

Figure 14. Comparison of experimental and computed results for special moment frame (SMF) specimen.

tional model agrees with the deformed shape shown in the photograph.

The computed vertical load reached a peak value of 163 kip (725 kN), within 2% of the experimental peak load at a center column displacement Δ of 5.8 in. (147 mm). After reaching this peak value, the vertical load dropped sharply because of anchorage bar fracture (**Fig. 13**). Fracture of the anchorage bars resulted from a combination of bending moment and axial tension, and significant out-of-plane bending of the link plates and anchorage bars is evident in Fig. 13, as was previously noted in Fig. 10.

Figure 13 shows the interaction of the computed axial force and bending moment in the lowest anchorage bar on the left side of the center column, in the critical element adjacent to the weld, where the initial fracture occurred. Figure 13 also shows limiting interaction boundaries corresponding to the yield strength f_y and the ultimate strength f_u of a no. 10 (32M) bar for reference, calculated based on chapter H of the 2010 AISC specification,[17] where the yield moment M_y equals Sf_y, (where S is the elastic section modulus), the yield capacity in tension T_y equals Af_y (where A is the cross-sectional area), the ultimate moment M_u equals Zf_u (where Z is the plastic section modulus), and the ultimate capacity in tension T_u equals Af_u. The limiting interaction boundaries in Fig. 13 correspond yield and ultimate strength values f_y of 64 ksi (441 MPa) and f_u of 90 ksi (621 MPa), obtained from tensile testing of a no. 10 (32M) bar.[7] Unloading and reloading of the anchorage bar, which occurred before fracture (Fig. 13), was caused by the failure of shear studs. The final fracture point was slightly beyond the limiting interaction boundary corresponding to the ultimate strength. The tensile force at fracture was 84% of the ultimate tensile capacity, indicating a moderate reduction in tensile strength due to moment-axial interaction.

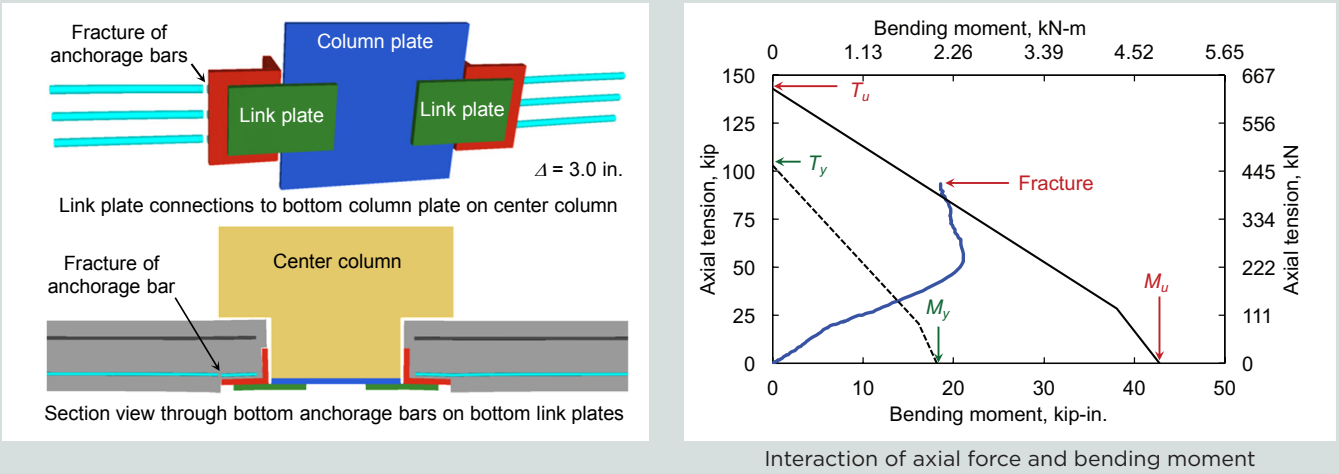

Figure 15. Anchorage bar fracture in special moment frame model. Note: M_u = ultimate moment; M_y = yield moment; T_u = ultimate capacity in tension; T_y = yield capacity in tension; Δ = vertical displacement. 1 in. = 25.4 mm.

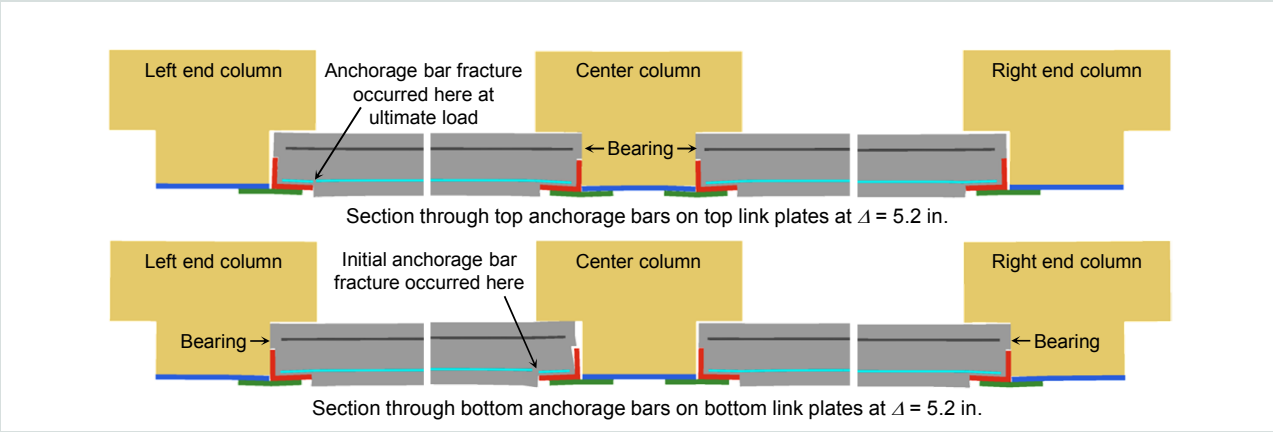

Figure 16. Section views of special moment frame model near the peak vertical load. Note: Δ = vertical displacement. 1 in. = 25.4 mm.

Special moment frame damage

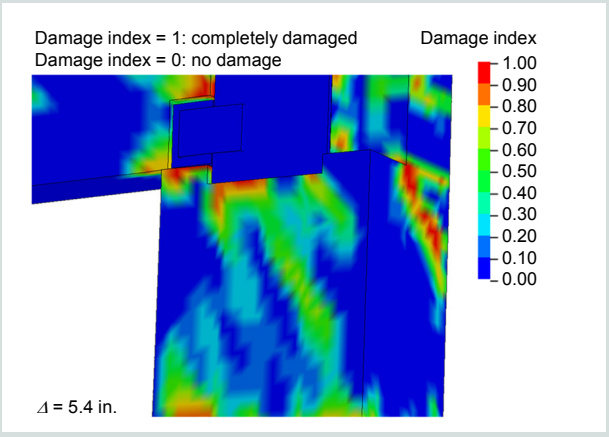

Contours of computed damage index

Figure 17. Concrete damage on right end column of special moment frame specimen. Note: Δ = vertical displacement. 1 in. = 25.4 mm.

The tensile force in the anchorage bar at fracture was within 1% of the peak axial force calculated from strain gauge measurements,[7] showing excellent agreement between the experimental and computed fracture points.

Special moment frame specimen

Figure 14 shows a comparison between the measured and computed curves of the applied vertical load and the horizontal reaction force at the end column tops for the special moment frame specimen, both plotted against the vertical displacement of the center column. Inward horizontal reaction forces are considered positive in Fig. 14, corresponding to tension in the brace beams spanning between the tops of the end columns. The experimental curve for the horizontal force in Fig. 14 was obtained as the sum of the axial forces in the front and back brace beams calculated from the measured strain data. The curve computed from the model for the horizontal force in Fig. 14 was obtained as the average of the horizontal reaction forces at the tops of the two end columns, with inward forces positive. An outward horizontal reaction developed in the initial application of self-weight in the computational model, and for consistency with the experimental measurements, this initial reaction was deducted from the horizontal force values in Fig. 14.

Figure 14 shows that the vertical load from the computational model reached an initial peak value of 163 kip (725 kN) at a vertical displacement of 2.8 in. (71 mm), before dropping sharply because of anchorage bar fracture (**Fig. 15**). A corresponding drop in load is also evident in the computed horizontal reaction at the column tops in Fig. 14. The measured and computed horizontal forces in Fig. 14 agree initially, both showing outward horizontal reactions corresponding to compressive brace forces. However, when the specimen was unloaded and

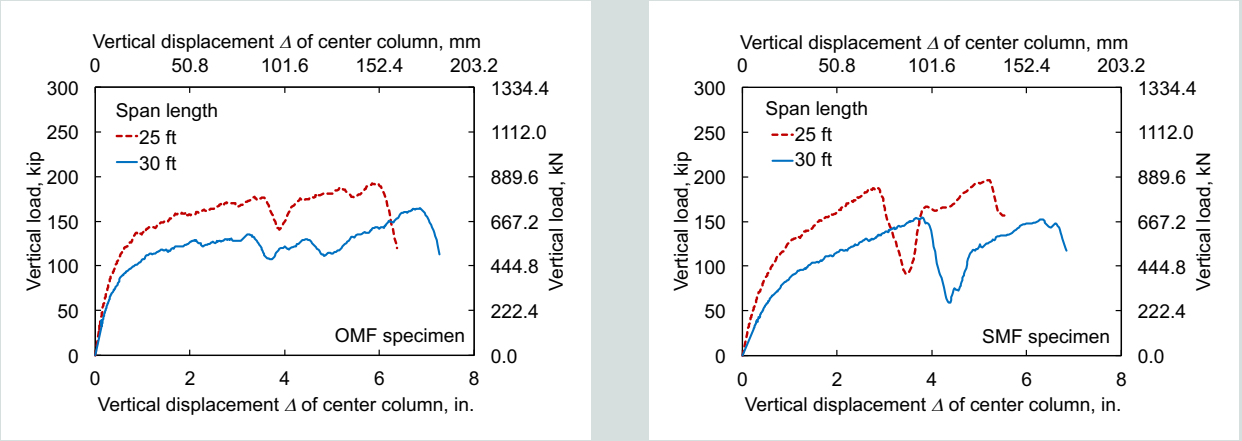

Figure 18. Influence of span length on computed vertical load-displacement response. Note: OMF = ordinary moment frame; SMF = special moment frame. 1 ft = 0.305 m.

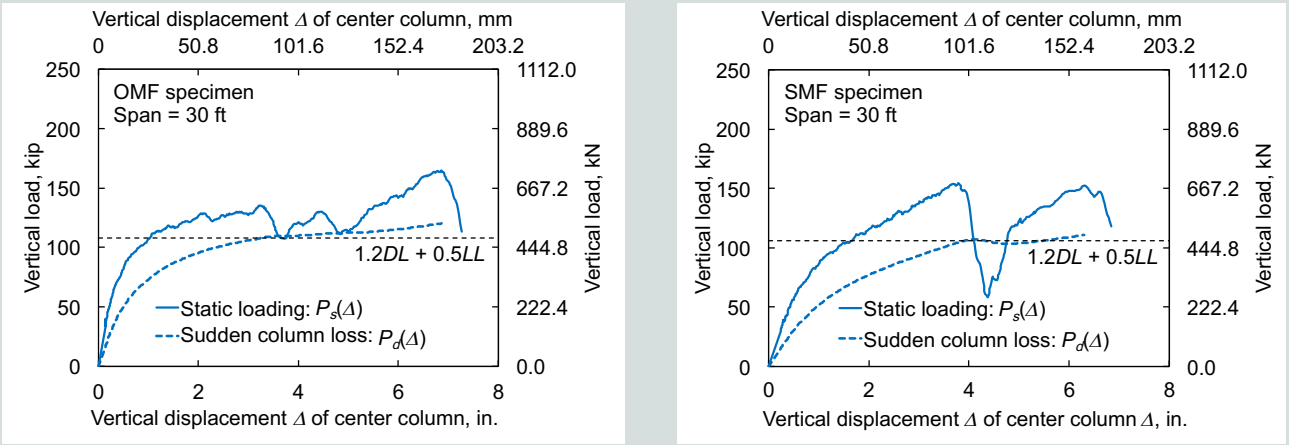

Figure 19. Load-displacement relationships for static loading and sudden column loss compared with applicable gravity loads. Note: *DL* = dead load; *LL* = live load; OMF = ordinary moment frame; $P_d(\Delta)$ = load as a function of column displacement including dynamic effects of sudden column loss; $P_s(\Delta)$ = load as a function of column displacement for static loading; SMF = special moment frame. 1 ft = 0.305 m.

reloaded after the initial phase of loading, the measured horizontal force never again reached the peak horizontal force of 43 kip (190 kN) attained in the initial loading. The unloading and reloading cycle appears to have introduced some change in the horizontal restraint that was not captured by the computational model (which was not unloaded and reloaded), and consequently, the peak computed horizontal force exceeded the measured value by 42%.

The three anchorage bars fractured nearly simultaneously in the model, in contrast with the experiment, in which the lowest anchorage bar fractured first at Δ equal to 2.5 in. (64 mm) and the upper two anchorage bars fractured later at Δ equal to 4.9 in. (124 mm). These differences in the experimentally observed fracture points may be due to variations in the ductility of the anchorage bars in the heat-affected zones near the welds, whereas the model assumed the same ductility for all anchorage bars.

Fracture of the anchorage bars resulted from a combination of bending moment and axial tension, and out-of-plane bending of the link plates and anchorage bars is evident in Fig. 15, though not as pronounced as it was for the ordinary moment frame specimen in Fig. 13. Figure 15 shows the interaction of the computed bending moment and axial force in the lowest anchorage bar on the left side of the center column, in the critical element adjacent to the weld, where fracture occurred. Due to the larger bar size, computed values of bending moment in the anchorage bar are larger for the special moment frame specimen in Fig. 15 than for the ordinary moment frame specimen in Fig. 13. Figure 15 also shows limiting interaction boundaries corresponding to yield

and ultimate strength values f_y of 68 ksi (469 MPa) and f_u of 95 ksi (655 MPa), obtained from tensile testing of a no. 11 (36M) bar.[7] The final fracture point was slightly beyond the limiting interaction boundary corresponding to the ultimate strength. The tensile force at fracture was 66% of the ultimate tensile capacity, indicating a significant reduction in capacity that resulted from the combined effects of moment-axial interaction and reductions in ductility of the bar in the heat-affected zone near the weld.

After fracture of the anchorage bars, the special moment frame specimen developed additional load-carrying capacity through arching action, with the top ends of the beams bearing against the center column and the bottom ends of the beams bearing against the end columns (**Fig. 16**). Outward forces from bearing of the beams against the end columns resulted in inclined damage contours in the lower portions of the end columns (**Fig. 17**), indicating the formation of diagonal shear cracks consistent with the experimental observations in Fig. 17.

The computed vertical load eventually reached an ultimate peak value of 172 kip (765 kN), about 8% less than the experimental peak, at a center column displacement at ultimate load Δ_u of 5.1 in. (130 mm) (Fig. 14). The vertical load dropped sharply after reaching the peak value, and a corresponding drop in the horizontal reaction force at the column tops is also evident in Fig. 14. Consistent with the experimental measurements, the horizontal reaction force changed direction from outward to inward after the peak vertical load as arching action began to force the tops of the end columns outward. In the computational model, the failure mode associated with the peak vertical load was fracture of the upper anchorage bars at the left end column (Fig. 16). In the experiment, the failure mode associated with the peak vertical load was bond failure of the upper anchorage bars at the right end column, which resulted from the formation of splitting cracks and spalling of the concrete cover.

The modeling approach used in this study is unable to capture this failure mode. While bond slip and bond failure could be modeled using a one-dimensional contact interface between the reinforcing bar and the surrounding concrete,[17] such an approach does not capture the influence of discrete crack formation on bond strength, which played an important role in this case. However, while the computational model indicated bar fracture rather than bond failure at the peak vertical load, the model correctly indicated that the failure mode involved the upper anchorage bars at an end column. The computed center column displacement at the peak load was about 22% less than the experimental value. The earlier failure of the upper anchorage bars in the model suggests that these bars may have been more ductile than was assumed. While all anchorage bars in the model were assumed to have the same ductility, the potential for significant variability in weld-induced reductions in ductility was noted previously.

Influence of span length

The span length of the test specimens was reduced to 25 ft (7.6 m), from the prototype span length of 30 ft (9 m), to fit within the testing facility. Somewhat smaller capacities would be expected if the full span length had been used in the test specimens. To investigate the influence of span length, finite element models of each specimen were developed in which the span length was increased to 30 ft. Apart from the difference in span length, the models were identical to the final posttest models of each specimen (models OMF-A and SMF-A in Table 1).

Figure 18 shows a comparison of the vertical load-displacement curves computed from the two finite element models of each specimen. Because the self-weight differed for the different span lengths, the vertical load values in Fig. 18 include the self-weight sustained by the specimens in addition to the load applied to the center column. Only self-weight that was tributary to the center column, which included the center column and half of each spandrel beam, was added.

For the 25 ft (7.6 m) span length, this self-weight amounted to 29.3 kip (130 kN) for the ordinary moment frame specimen and 24.9 kip (111 kN) for the special moment frame specimen, and the vertical load values in Fig. 18 are thus greater than the corresponding values in Fig. 9 and 14 by these respective amounts. For the 30 ft (9 m) span length, the self-weight amounted to 33.8 kip (150 kN) for the ordinary moment frame specimen and 28.8 kip (128 kN) for the special moment frame specimen. The displacement values in Fig. 18 include displacements due to self-weight in addition to the computed displacements due to loading of the center column.

The behaviors and failure modes observed in the computational models with the 30 ft (9 m) span length were essentially the same as those described previously for the 25 ft (7.6 m) span length. However, Fig. 18 shows that the longer-span specimens had lower ultimate capacities that were achieved at larger vertical displacements of the center column, with the ultimate capacity of the special moment frame specimen being slightly less than that of the ordinary moment frame specimen for the prototype span length. The ultimate capacities for the prototype span length were 165 and 155 kip (733 and 688 kN) for the ordinary moment frame and special moment frame specimens, respectively, occurring at displacements at ultimate loads Δ_u of 6.9 in. (175 mm) and 6.3 in. (160 mm). These ultimate capacities represent a reduction relative to the shorter-span capacities (including self-weight) by

14% for the ordinary moment frame specimen and by 21% for the special moment frame specimen.

For the special moment frame specimen, the influence of arching action was less significant for the longer span length so that the ultimate peak load at Δ_u of 6.3 in. (160 mm) was essentially equivalent to the initial peak load at Δ of 3.8 in. (96 mm). The center column displacement at the ultimate load Δ_u was larger for the longer span length than for the shorter span length by 17% for the ordinary moment frame specimen and by 22% for the special moment frame specimen. However, the beam chord rotation at the ultimate load θ_u, given by $\tan^{-1}(\Delta_u/L)$, where L is the span length between column centerlines, was nearly equivalent for both span lengths, differing by 2% for the ordinary moment frame specimen and by 1% for the special moment frame specimen.

Evaluation of structural robustness

The structural robustness of the precast concrete moment-frame assemblies was evaluated through a comparison of their ultimate capacities with the applicable gravity loads from the prototype buildings using an energy-based procedure to account for the dynamic effects of sudden column loss. Computational results for specimens with the full prototype span length of 30 ft (9 m) were used in the evaluation to account for the reduction in capacities associated with the longer span length and to enable a direct comparison with gravity loads from the prototype buildings.

Gravity loads

Applicable gravity loads were based on the load combination of $1.2DL + 0.5LL$, where DL is dead load and LL is live load. This corresponds to the load combination specified in ASCE 7-10 section 2.5.2.2[18] for evaluating the residual capacity of structural systems following the notional removal of load-bearing elements. A live load of 50 lb/ft^2 (2.4 kN/m^2) was considered, corresponding to office occupancy, with a live load reduction factor of 0.75 based on Eq. (4.7-1) in ASCE 7-10, resulting in a reduced live load 37.5 lb/ft^2 (1.80 kN/m^2). Multiplying by the tributary area of 450 ft^2 (41 m^2) for an edge column yields an unfactored live load of 16.9 kip (75.1 kN) acting on the column to be removed.

The dead load acting on the column to be removed included self-weight plus a superimposed dead load of 10 lb/ft^2 (0.5 kN/m^2). The unfactored dead load corresponding to the tributary area of the column to be removed was estimated from the design documents as 83 kip (369 kN) for the ordinary moment frame building and 81 kip (360 kN) for the special moment frame building.[7] Applying load factors for the selected load combination yielded total gravity loads of 108 kip (481 kN) and 106 kip (470 kN) acting on the column to be removed for the ordinary moment frame assembly and the special moment frame assembly, respectively.

Energy-based analysis

Figure 19 shows load-displacement curves for the two moment-frame assemblies for both static loading and sudden column loss. The static load-displacement curves were obtained from the computational models and are equivalent to the curves presented in Fig. 18 for the 30 ft (9 m) span length. The curves for sudden column loss were calculated from the static load-displacement curves according to the following equation, based on the energy balance between the internal energy in the structure and the external work done by gravity loads at the peak displacement following a sudden column loss.[19–21] This equation is further explained and illustrated by Main et al.[7]

$$P_d(\Delta) = \frac{1}{\Delta}\int_0^{\Delta} P_s(\tilde{\Delta})\, d\tilde{\Delta}$$

where

$P_d(\Delta)$ = load as a function of column displacement including dynamic effects of sudden column loss

$P_s(\Delta)$ = load as a function of column displacement for static loading

$\tilde{\Delta}$ = integration variable representing the vertical column displacement

The dashed horizontal lines in Fig. 19 correspond to the applicable gravity load combination, and the intersection of the curve for $P_d(\Delta)$ with the dashed horizontal line in each plot gives the peak dynamic displacement under sudden column loss for this level of gravity loading. Peak dynamic displacements of 3.3 and 3.9 in. (83 and 100 mm) were obtained for the ordinary moment frame specimen and the special moment frame specimen, respectively. The analyses thus predicted that both precast concrete specimens could sustain the applicable gravity loads under sudden column loss without collapse. For both specimens, however, the curves for $P_d(\Delta)$ exceeded the applicable gravity load combination only slightly, and the predicted displacements under sudden column loss were highly sensitive to further increases in the gravity loading.

Normalized ultimate capacities

A normalized measure of the ultimate capacity under static loading $\lambda_{s,u}$ can be obtained by dividing the ultimate static capacity by the applicable gravity loading $1.2DL + 0.5LL$. Values for $\lambda_{s,u}$ of 1.53 and 1.46 were ob-

tained for the ordinary moment frame and special moment frame specimens, respectively, indicating that the specimens could sustain static loads exceeding the applicable gravity loads by about 50%. Ultimate capacities under sudden column loss were calculated at the displacement corresponding to the ultimate static load, as proposed by Main,[23] and ultimate capacities $P_d(\Delta_u)$ of 120 and 108 kip (535 and 479 kN) were obtained for the ordinary moment frame and special moment frame specimens, respectively. Dividing these values by the applicable gravity loading yields normalized values of the ultimate capacity under sudden column loss $\lambda_{d,u}$.

The quantity $\lambda_{d,u}$ was proposed by Bao et al.[22] as a robustness index for structural systems, where values greater than unity indicate that a structure will not collapse under sudden column loss. Using this approach, robustness indices $\lambda_{d,u}$ of 1.11 and 1.02 were obtained for the ordinary moment frame and special moment frame specimens, respectively. This indicates that the precast concrete specimens could sustain loads 2% to 11% greater than the applicable gravity loads under sudden column loss. The dynamic increase factor at the ultimate static load is defined as the ratio of $\lambda_{s,u}$ to $\lambda_{d,u}$, and values of 1.37 and 1.43 were calculated for the ordinary moment frame and special moment frame specimen, respectively. This indicates that in a nonlinear static analysis, the loads on the precast concrete frames would need to be increased by about 40% to account for the dynamic effects of sudden column loss.

Discussion

The computed results indicated reserve capacities of 2% to 11% against collapse for the prototype span length. These reserve capacities, however, are comparable to the uncertainty in the model predictions. Differences of 2% to 8% were observed between the computed and experimental ultimate capacities for the reduced span length, and somewhat larger discrepancies would be expected when extending the models to the full prototype span length.

In addition, the computed responses were found to be sensitive to factors such as the initial gap width between the beams and columns (which was not specified in the design) and the ductility of the welded anchorage bars. Variations in these factors were found to reduce the computed ultimate capacities by 35%. Differences in these factors were observed between the two specimens that were tested, with larger gap widths for the ordinary moment frame specimen and greater reductions in anchorage bar ductility for the special moment frame specimen. Additional variability in the test specimens was introduced by installation errors for the special moment frame specimen, though computational modeling showed that these errors reduced the ultimate capacity by only about 4%. Because of the strong sensitivities observed, significant variability might be expected if multiple tests of nominally identical specimens were tested and some combinations of factors could result in specimens that would not sustain the applicable gravity loads under sudden column loss.

Although the special moment frame specimen was designed under more stringent seismic requirements than the ordinary moment frame specimen, the computational models predicted that for the full prototype span length, the ultimate capacities of the two specimens were approximately equivalent, with the special moment frame specimen having a slightly smaller capacity. The comparable performance of the ordinary moment frame and special moment frame specimens contrasts with previous full-scale testing of steel moment frames[10] and cast-in-place concrete moment frames,[17] in which the ultimate capacity of special moment frame specimens under a column removal scenario was approximately twice the ultimate capacity of corresponding intermediate moment frame specimens.

Because the design and detailing requirements for an ordinary moment frame are less stringent than for a seismically designed intermediate moment frame, significant improvements in performance might have been expected for a special moment frame specimen relative to an ordinary moment frame specimen. Earlier fracture of the welded anchorage bars was a key factor that reduced the capacity of the special moment frame specimen relative to the ordinary moment frame specimen. While the steel and cast-in-place concrete moment frames resisted loads through catenary action,[10,17] catenary action did not develop in the precast concrete moment frames because failures depleted the capacity of the specimens when the center column displacement remained much less than the depth of the spandrel beams.

For a column removal scenario in an actual building, the response of a precast concrete moment frame would depend on the resistance provided by the surrounding structural system, which would vary depending on the location within the building. This study considered end columns with spandrel beams framing into the connections from only one side. Spandrel beams framing into the columns from both sides would provide additional resistance to rotation and horizontal displacement of the columns, thus reducing the flexural and shear demands on the columns and providing increased support for the development of compressive arching action. The floor system may also provide additional restraint to the columns.

Axial forces in the columns due to gravity loads from the upper stories, while increasing the stress levels in the columns, would also provide increased resistance to shear forces resulting from arching action. In a corner column removal scenario, however, negligible arching action would be expected because of the limited horizon-

tal restraint of the corner column. These issues and other influences of the surrounding structural system on the robustness of precast concrete moment frames can be investigated in future studies using computational modeling.

Conclusion

This paper presented computational modeling and analysis of precast concrete ordinary moment frame and special moment frame specimens subjected to displacement-controlled vertical loading of an unsupported center column, simulating a column removal scenario. The analyses conducted using these models captured the primary response characteristics of the test specimens and provided insights into the overall behavior and failure modes. Based on the analysis results reported herein, the following main conclusions were reached:

- The responses of the specimens were found to be sensitive to the following key factors: the width of the initial gap between the spandrel beams and columns, the reduction in ductility of the welded anchorage bars in the heat-affected zone near the welds, and the reduction in the effective shear strength of the shear studs due to out-of-plane bending of the link plates. Sensitivity to these factors, which were not well known prior to the tests, contributed to overestimation of the capacities by the pretest models.

- Fracture of welded anchorage bars, which contributed to the failure of both specimens, occurred earlier than would be expected under purely tensile loading because of local bending moments near the welds that resulted from eccentricities in the transfer of forces through the link plate connections. For the special moment frame specimen, component testing and detailed modeling of a welded anchorage bar showed that weld-induced reductions in ductility also influenced these failures. Computational models of the test specimens showed that because of these effects, fracture of the anchorage bars occurred at 84% of the ultimate tensile capacity of the anchorage bar for the ordinary moment frame specimen and at 66% of the ultimate tensile capacity for the special moment frame specimen.

- Shear stud failures at the upper link plate connections to the end columns of the ordinary moment frame specimen were influenced by out-of-plane bending of the link plates, which resulted in a complex interaction of stresses that significantly reduced the effective shear capacity of the shear studs. Further research would be required to develop a mechanics-based failure model for the shear studs that explicitly accounted for this complex interaction of stresses. In this study, the effects of out-of-plane bending were accounted for by reducing the effective shear strength of each shear stud to approximately 30% of its nominal value. In contrast with other aspects of the modeling, which were based on constitutive relationships for the various materials, the failure criterion for the shear studs was calibrated to capture the experimentally observed failures.

- The computational models captured the arching action that was observed for both specimens in which increased vertical loads were developed through bearing forces between the spandrel beams and columns. Because of arching action, the vertical loads sustained by the moment-frame assemblies were found to be strongly influenced by the width of the initial gaps between the beams and columns, particularly for the ordinary moment frame specimen, which had deeper spandrel beams. Inclined damage contours in the lower portion of the end columns became evident after the development of arching action, indicating the formation of diagonal shear cracks consistent with the experimental observations. Catenary action did not develop in either specimen.

- The test specimens had a reduced span length of 25 ft (7.6 m), and computational modeling showed that considering the full prototype span length of 30 ft (9.1 m) reduced the ultimate capacity by 14% for the ordinary moment frame specimen and by 21% for the special moment frame specimen. The ultimate capacities of the prototype-span specimens under static loading exceeded the applicable gravity loading of $1.2DL + 0.5LL$ by factors of 1.53 and 1.46 for the ordinary moment frame and special moment frame specimens, respectively. Ultimate capacities of the prototype-span specimens under sudden column loss were evaluated using an approximate energy-based procedure, and the resulting values slightly exceeded the applicable gravity loads by 11% and 2% for the ordinary moment frame and special moment frame specimens, respectively. However, given the observed sensitivity of the results to factors such as the initial gap width between the beams and columns and the weld-induced reductions in ductility of the anchorage bars, variations in these factors could result in specimens that would not sustain the applicable gravity loads under sudden column loss. The computational results indicated that for the full prototype span length, the ultimate capacity of the special moment frame specimen under the column removal scenario was approximately equivalent to that of the ordinary moment frame specimen, despite the more stringent design requirements.

Acknowledgments

The authors gratefully acknowledge Zhiyu Zong's contribution to the finite element model development while a

guest researcher at NIST and the thorough review of this work by Jonathan M. Weigand of NIST and David J. Stevens of Protection Engineering Consultants.

References

1. Bao, Y., S. Kunnath, S. El-Tawil, and H. S. Lew. 2008. "Macromodel-Based Simulation of Progressive Collapse: RC Frame Structures." *Journal of Structural Engineering* 134 (7): 1079–1091.

2. Sasani, M., A. Werner, and A. Kazemi. 2011. "Bar Fracture Modeling in Progressive Collapse Analysis of Reinforced Concrete Structures." *Engineering Structures* 33 (2): 401–409.

3. Sadek, F., J. A. Main, H. S. Lew, and S. El-Tawil. 2013. "Performance of Steel Moment Connections under a Column Removal Scenario. II: Analysis." *Journal of Structural Engineering* 139 (1): 108–119.

4. Yu, J., and K. H. Tan. 2013. "Experimental and Numerical Investigation on Progressive Collapse Resistance of Reinforced Concrete Beam Column Subassemblies." *Engineering Structures*, no. 55: 90–106.

5. Bao, Y., H. S. Lew, and S. Kunnath. 2014. "Modeling of Reinforced Concrete Assemblies under Column-Removal Scenario." *Journal of Structural Engineering* 140 (1): 04013026. doi:10.1061/(ASCE)ST.1943-541X.0000773.

6. Lew, H. S., J. A. Main, Y. Bao, F. Sadek, V. P. Chiarito, S. D. Robert, and J. O. Torres. 2017. "Performance of Precast Concrete Moment Frames Subjected to Column Removal: Part 1, Experimental Study." *PCI Journal* 62 (5): 35–52.

7. Main, J. A., Y. Bao, H. S. Lew, F. Sadek, V. Chiarito, S. D. Robert, and J. Torres. 2015. "An Experimental and Computational Study of Precast Concrete Moment Frames under a Column Removal Scenario." NIST (National Institute of Standards and Technology) Technical Note 1886. Gaithersburg, MD: NIST.

8. Murray, Y. D., A. Abu-Odeh, and R. Bligh. 2007. "Evaluation of LS-DYNA Concrete Material Model 159." FHWA-HRT-05-063. McLean, VA: Federal Highway Administration.

9. ASTM International. 2008. *Standard Specification for Carbon Structural Steel*. ASTM A36/A36M–08. West Conshohocken, PA: ASTM.

10. Sadek, F., J. A. Main, H. S. Lew, S. D. Roberts, V. P. Chiarito, and S. El-Twail. 2010. "An Experimental and Computational Study of Steel Moment Connections under a Column Removal Scenario." NIST Technical Note 1669. Gaithersburg, MD: NIST.

11. ASTM International. 2016. *Standard Specification for Deformed and Plain Low-Alloy Steel Bars for Concrete Reinforcement*. ASTM A706/A706M–16. West Conshohocken, PA: ASTM.

12. ASTM International. 2016 *Standard Specification for Alloy-Steel and Stainless Steel Bolting for High Temperature or High Pressure Service and Other Special Purpose Applications*. ASTM A193/A193M–16. West Conshohocken, PA: ASTM.

13. PCI Industry Handbook Committee. 2014. *PCI Design Handbook: Precast and Prestressed Concrete*. MNL-120. 7th ed. Chicago, IL: PCI.

14. Ollgaard, J. G., R. G. Slutter, and J. W. Fisher. 1971. "Shear Strength of Stud Connectors in Lightweight and Normal Weight Concrete." *Engineering Journal* 8 (2): 55–64.

15. AISC (American Institute of Steel Construction). 2010. *Specification for Structural Steel Buildings*. ANSI (American National Standards Institute)/AISC 360-10. Chicago, IL: AISC.

16. AWS (American Welding Society). 2010. *Structural Welding Code –Steel*. AWS D1.1/D1.1M:2010. Miami, FL: AWS.

17. Lew, H. S., Y. Bao, F. Sadek, J. A. Main, S. Pujol, and M. A. Sozen. 2011. "An Experimental and Computational Study of Reinforced Concrete Assemblies under a Column Removal Scenario." NIST Technical Note 1720. Gaithersburg, MD: NIST.

18. ASCE (American Society of Civil Engineers). 2010. *Minimum Design Loads for Buildings and Other Structures*. SEI (Structural Engineering Institute)/ASCE 7-10. Reston, VA: ASCE.

19. Powell, G. "Collapse Analysis Made Easy (More or Less)." Paper presented at the Annual Meeting of the Los Angeles Tall Buildings Structural Design Council: Progressive Collapse and Blast Resistant Design of Buildings, Los Angeles, CA, May 2003.

20. Izzuddin, B. A., A. G. Vlassis, A. Y. Elghazouli, and D. A. Nethercot. 2008. "Progressive Collapse of Multi-storey Buildings Due to Sudden Column Loss–Part I: Simplified Assessment Framework." *Engineering Structures*, no. 30: 1308–1318.

21. Main, J. A. 2014. "Composite Floor Systems under Column Loss: Collapse Resistance and Tie Force Requirements." *Journal of Structural Engineering* 140 (8): A4014003.

22. Bao, Y., J. A. Main, and S. Y. Noh. 2017. "Evaluation of Structural Robustness against Column Loss: Methodology and Application to RC Frame Buildings." *Journal of Structural Engineering* 143 (8): 04017066.

Notation

A = cross-sectional area of reinforcing bar

DL = dead load

f_u = ultimate strength

f_y = yield strength

L = span length between column centerlines

LL = live load

M_u = ultimate moment

M_y = yield moment

$P_d(\Delta)$ = load as a function of column displacement including dynamic effects of sudden column loss

$P_s(\Delta)$ = load as a function of column displacement for static loading

Q_n = nominal shear strength of shear stud connector

S = elastic section modulus

T_u = ultimate capacity in tension

T_y = yield capacity in tension

Z = plastic section modulus

Δ = vertical displacement

Δ_u = vertical displacement of center column at the ultimate load

$\tilde{\Delta}$ = integration variable representing the vertical column displacement

θ_u = chord rotation at the ultimate load

$\lambda_{d,u}$ = normalized ultimate capacity under sudden column loss = robustness index

$\lambda_{s,u}$ = normalized ultimate capacity under static loading

About the authors

Yihai Bao, PhD, is an Intergovernmental Personnel Act researcher in the Engineering Laboratory at NIST. He received his BS and MS degrees from Tongji University in China and his PhD from the University of California, Davis. His research interests include nonlinear modeling of structural behavior under extreme loading conditions, large-scale experimental methods, and advanced scientific computational methods.

Joseph Main, PhD, is a research structural engineer in the Engineering Laboratory at NIST. He received his PhD from Johns Hopkins University in Baltimore, Md. His research interests relate to the computational assessment of structural performance under extreme loads, including wind loading, air-blast loading, and loading generated by abnormal events, such as fire, explosions, and vehicular impacts.

H. S. Lew, PE, PhD, Honorary Member ACI, is a senior research engineer in the Engineering Laboratory at NIST. He received his PhD from the University of Texas at Austin. He has served on the ACI Board of Direction and the Technical Activities Committee. He is a member of ACI Committee 318, Concrete Research Council, and other ACI committees. His research interests include performance of structural members and systems, construction safety, failure investigations, and earthquake engineering.

Fahim Sadek, PE, PhD, is a research structural engineer in the Engineering Laboratory at NIST. He received his PhD from Southern Methodist University in Dallas, Tex. His research interests include vulnerability of structures subjected to multihazard conditions, response of structures to dynamic and impulse loading, and structural health monitoring.

Abstract

This paper presents a computational study of two precast concrete moment-frame assemblies, each comprising three columns and two beams, subjected to displacement-controlled vertical loading of the unsupported center column to simulate a column removal scenario. One assembly was part of an ordinary moment frame, and the other was part of a special moment frame. Finite element models of each assembly were developed to capture the experimentally observed behaviors and failure modes; provide additional insights into behaviors and failure modes that could not be directly observed from the experimental data, including the sensitivity of the responses to variations in key factors; and evaluate the structural robustness of the two assemblies by comparing their ultimate capacities with the applicable gravity loading, including the dynamic effects associated with sudden column loss.

Keywords

Building, column, connection, disproportionate collapse, finite element model, moment-resisting connection, structural robustness.

Review policy

This paper was reviewed in accordance with the Precast/Prestressed Concrete Institute's peer-review process.

Reader comments

Please address reader comments to journal@pci.org or Precast/Prestressed Concrete Institute, c/o *PCI Journal*, 200 W. Adams St., Suite 2100, Chicago, IL 60606.